Monthly Notices of the ROYAL ASTRONOMICAL SOCIETY

MNRAS **517,** 2471–2484 (2022) https://doi.org/10.1093/mnras/stac2748
Advance Access publication 2022 September 27

Non-universal stellar initial mass functions: large uncertainties in star formation rates at $z \approx 2$–4 and other astrophysical probes

Joshua J. Ziegler [1★] Thomas D. P. Edwards,[2,3,4] Anna M. Suliga,[5,6,7] Irene Tamborra,[7] Shunsaku Horiuchi [8,9] Shin'ichiro Ando[2,9] and Katherine Freese[1,3,4]

[1]*Department of Physics, University of Texas at Austin, Austin, TX 78712, USA*
[2]*Gravitation Astroparticle Physics Amsterdam (GRAPPA), Institute for Theoretical Physics Amsterdam and Delta Institute for Theoretical Physics, University of Amsterdam, Science Park 904, NL-1090 GL Amsterdam, the Netherlands*
[3]*The Oskar Klein Centre, Department of Physics, Stockholm University, AlbaNova, SE-10691 Stockholm, Sweden*
[4]*Nordic Institute for Theoretical Physics (NORDITA), SE-106 91 Stockholm, Sweden*
[5]*Department of Physics, University of California Berkeley, Berkeley, CA 94720, USA*
[6]*Department of Physics, University of Wisconsin-Madison, Madison, WI 53706, USA*
[7]*Niels Bohr International Academy and DARK, Niels Bohr Institute, University of Copenhagen, Blegdamsvej 17, DK-2100 Copenhagen, Denmark*
[8]*Center for Neutrino Physics, Department of Physics, Virginia Tech, Blacksburg, VA 24061, USA*
[9]*Kavli IPMU (WPI), UTIAS, The University of Tokyo, Kashiwa, Chiba 277-8583, Japan*

Accepted 2022 September 21. Received 2022 September 20; in original form 2022 June 9

ABSTRACT

We explore the assumption, widely used in many astrophysical calculations, that the stellar initial mass function (IMF) is universal across all galaxies. By considering both a canonical broken-power-law IMF and a non-universal IMF, we are able to compare the effect of different IMFs on multiple observables and derived quantities in astrophysics. Specifically, we consider a non-universal IMF that varies as a function of the local star formation rate, and explore the effects on the star formation rate density (SFRD), the extragalactic background light, the supernova (both core-collapse and thermonuclear) rates, and the diffuse supernova neutrino background. Our most interesting result is that our adopted varying IMF leads to much greater uncertainty on the SFRD at $z \approx 2-4$ than is usually assumed. Indeed, we find an SFRD (inferred using observed galaxy luminosity distributions) that is a factor of $\gtrsim 3$ lower than canonical results obtained using a universal IMF. Secondly, the non-universal IMF we explore implies a reduction in the supernova core-collapse rate of a factor of ~ 2, compared against a universal IMF. The other potential tracers are only slightly affected by changes to the properties of the IMF. We find that currently available data do not provide a clear preference for universal or non-universal IMF. However, improvements to measurements of the star formation rate and core-collapse supernova rate at redshifts $z \gtrsim 2$ may offer the best prospects for discernment.

Key words: stars: formation – stars: luminosity function, mass function – supernovae: general – galaxies: luminosity function, mass function – neutrinos – methods: data analysis.

1 INTRODUCTION

In order to understand the formation and evolution of stars, an important quantity is the stellar initial mass function (IMF), the relative numbers of stars as a function of their mass at the time of their formation. As yet, the IMF remains only loosely constrained observationally. A common assumption is that the IMF is universal – the same in all environments and throughout cosmic time. In this paper, we examine five observables that vary over cosmological distances and which strongly depend on the high-mass region of the IMF. One of our goals is to identify the extent to which these observables can be used to test the assumption of a universal IMF at the high-mass end. In particular, we study the consequences of non-universal IMFs for various astrophysical quantities, finding larger uncertainties in the star formation rate (SFR) and the core-collapse supernova rate.

The concept of an IMF was introduced by Salpeter (1955), who proposed a single power law $\frac{\mathrm{d}N}{\mathrm{d}M} \propto M^{\alpha}$, where N is the number of stars formed with mass M; in what is now known as the Salpeter IMF, he took $\alpha = -2.35$. With the assumption of a single power law, the exponent α can be measured to within approximately 10 per cent (Baldry & Glazebrook 2003). Unfortunately, there are fundamental questions about the parametrization that should be used in describing the IMF. Perhaps most notably, it was recognized at the end of the 20th century that low-mass stars did not tend to fall on the power-law distribution predicted by Salpeter. This gave rise to IMF models with low-mass suppressions, such as the broken power law of Kroupa (2001) and the lognormal distribution of Chabrier (2003). Recent evidence suggests that the IMF may even have an intrinsic dependence on the local environment (Harayama, Eisenhauer & Martins 2008; van Dokkum & Conroy 2010; Gunawardhana et al. 2011; Cappellari et al. 2012; Ferreras et al. 2012; Ferré-Mateu, Vazdekis & de la Rosa 2013; La Barbera et al. 2019). Variations to the low-mass end of the IMF have been studied extensively in the literature (Chabrier 2003; van Dokkum & Conroy 2010; Geha 2013).

★ E-mail: jjziegler@utexas.edu

Instead, following recent evidence (Gunawardhana et al. 2011), we focus on observables sensitive to the high-mass end of the IMF that may also be non-universal. Throughout this paper, we consider IMFs that are universal at low masses and vary only at high masses. The results of our analysis may therefore differ from analyses that consider IMFs with low-mass variations.

Star-forming regions can be distinguished by a variety of properties of the collapsing gas and dust, including angular momentum, metallicity, density, temperature, and dust content. The universality of the IMF therefore boils down to an assumption that all of these properties play little to no role in the masses of the formed stars. Whether this is theoretically justified remains unclear. As described in Offner et al. (2014, and references therein), perturbations in the density of a star-forming gas cloud can, under reasonable assumptions, generate a power-law spectrum of core and clump masses, where cores and clumps refer to gravitationally collapsing gas clouds that are likely to form at least one star. In contrast to this power-law distribution, at low masses, turbulence in the star-forming cloud can naturally produce a spectrum of masses that disfavours lower mass stars relative to the power-law predictions. In particular, Padoan, Nordlund & Jones (1997) showed that turbulence could give rise to a lognormal mass distribution among low-mass cores/clumps, similar to the IMF described by Chabrier (2003). While this theoretical explanation would seem to leave very little room for non-universality in the IMF, the mass function described here is for cores and clumps, not stars. In relating this mass function to the stellar IMF, numerous assumptions must be made about the formation of protostars out of collapsing gas (Offner et al. 2014). The validity of many of these assumptions, especially in extreme environments, is largely an open question, suggesting that even within this theoretical framework, there may be room to consider non-universality without requiring a new paradigm.

The question of whether the IMF is indeed universal has been investigated many times. For example, despite most observations being consistent with a universal IMF, authors have regularly suggested a non-universal IMF as a way to explain other astrophysical tensions (Larson 1998). Further, over the last two decades, hints of a tension between universal IMFs and observations have developed, particularly in early-type elliptical galaxies (van Dokkum & Conroy 2010; Cappellari et al. 2012; Ferreras et al. 2012; Ferré-Mateu et al. 2013; La Barbera et al. 2019) and in environments that experience extreme properties (Harayama et al. 2008; Gunawardhana et al. 2011). Theoretical models, such as the integrated galaxy-wide IMF (Kroupa & Weidner 2003; Fontanot et al. 2017; Jeřábková et al. 2018; Chruślińska et al. 2020) and the cosmic ray-regulated star formation discussed in Fontanot et al. (2018), can offer justifications for some of these observations and pose additional predictions. On the other hand, due to the inherent difficulty in measuring the IMF, many authors reject these observational claims, leaving the question of whether the IMF is indeed universal largely unanswered (see e.g. Hopkins 2018, and references within for a recent review of the range of perspectives).

A large part of the uncertainty in whether the IMF is universal can be traced to the difficulty in unambiguously measuring it. Locally, where it is possible to resolve individual stars, one can estimate the IMF by comparing observed stellar populations to the populations that are predicted to form if different IMF models are assumed (Kennicutt & Evans 2012; Calzetti 2013). While accurate, this approach can only be used in star-forming regions nearby enough to resolve individual stars, and requires assumptions about the history of star formation in that region. On the other hand, for more distant galaxies, where it is impossible to see inside star-forming regions or where it is difficult to resolve individual stars, some proxy for the SFR must be used. The most common approach is to use the luminosity as a measure of the rate of star formation (e.g. Kennicutt 1998), but this causes observations of the IMF to depend heavily on the calibration factor between luminosity and SFR. While it is possible to calculate this calibration factor numerically, it requires an assumption about the IMF. Unfortunately, this circular dependence encountered when calculating the IMF of distant galaxies is rather ubiquitous, making an independent measurement of the IMF challenging.

While it is difficult to directly measure the IMF, it may be possible to find indirect ways to probe the effects of a non-universal IMF. Previous works, such as Fontanot et al. (2017), Jeřábková et al. (2018), Chruślińska et al. (2020), and Fontanot et al. (2018) approach this problem as well, but use different models of varying IMF and probe different astrophysical observables than we do here.

In this paper, we examine five observables that vary over cosmological distances and which depend on the IMF: the star formation rate density (SFRD), the extragalactic background light (EBL), the core-collapse supernova (CCSN) rate density, the type Ia supernova (SNIa) rate, and the diffuse supernova neutrino background (DSNB). For each, we explore how they change when using a non-universal IMF compared to a universal one, and discuss whether they are discriminable with current or future data. For simplicity, we focus on the change induced by a varying IMF and ignore many other uncertainties directly related to each observable. These additional uncertainties will, in practice, make it more difficult to observe the IMF induced changes. Furthermore, by focusing on an IMF that only varies at high masses, we can explore only a subset of the possible effects that an IMF which varies at both high and low masses would predict. Our goal is simply to learn whether astrophysical observations of distant objects could, in principle, provide indirect evidence for a non-universal IMF.

The rest of this paper is structured as follows. In Section 2, we describe the two IMF models we consider throughout the paper. In Section 3, we look at how these IMF models affect the five quantities described in the previous paragraph: the SFRD, the EBL, the CCSN rate density, the SNIa rate, and the DSNB. Finally, we conclude in Section 4.

2 INITIAL MASS FUNCTION MODELS

In a star-forming region, the stellar IMF describes the distribution of masses with which stars form. A common approach to describing this IMF is through a probability distribution $\xi(M)$. That is

$$\frac{\mathrm{d}N}{\mathrm{d}M} = \xi(M) N_{\mathrm{tot}}, \tag{1}$$

where N is the number of stars formed with mass M, typically measured in units of $\mathrm{M}_{\odot}$, and N_{tot} is the total number of stars formed. Under this convention, $\xi(M)$ is normalized such that $\int \xi(M)\mathrm{d}M = 1$, when integrating over all possible stellar masses.

In Salpeter's seminal work (Salpeter 1955), the IMF was described as a power law of the form

$$\xi(M) \propto M^{\alpha}, \tag{2}$$

where $\alpha = -2.35$ was observed for stars in a mass range $0.4 - 1.0\,\mathrm{M}_{\odot}$. Since then, the range of masses over which the IMF could be determined has vastly increased, but the practice of describing the IMF through a power-law slope has remained. However, as IMFs have been studied, the single straight power law of Salpeter has given way to IMFs with more features. For example, commonly used IMFs include the piecewise power law established by Kroupa (2001; a

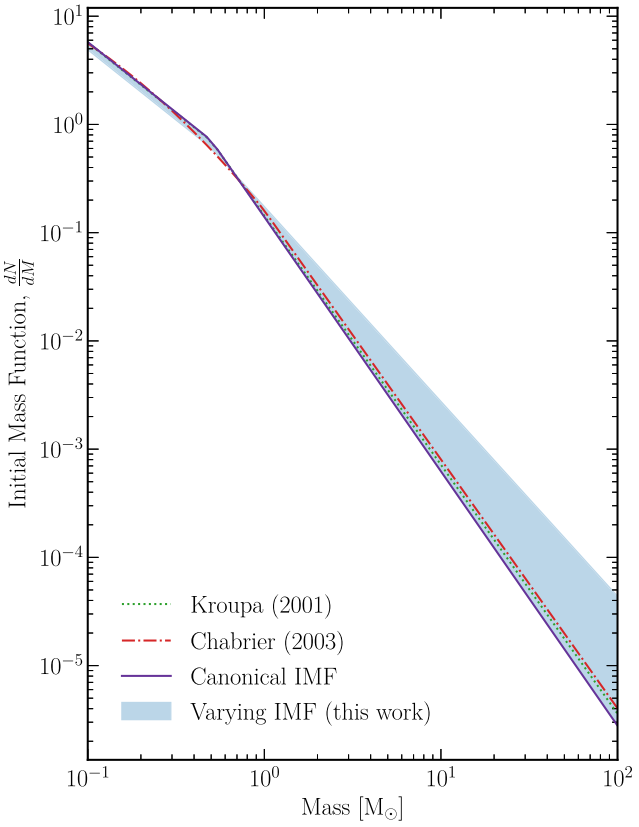

Figure 1. Initial mass functions: This figure compares the non-universal IMFs we use in this paper (blue shaded region) to the canonical IMFs used in the literature: Kroupa (2001; green dotted) and Chabrier (2003; red dash–dotted). We note the similarity of the two canonical cases relative to the wide range of non-universal IMFs we consider; we will use a proxy we identify as the *canonical* IMF (purple solid line) as our benchmark for the canonical cases. Each IMF is normalized so that the integral over mass equals 1. The Kroupa IMF follows a broken power law, with slope $\alpha = -1.3$ for $M < 0.5\,\mathrm{M}_\odot$ and $\alpha = -2.3$ for $M > 0.5\,\mathrm{M}_\odot$. The Chabrier IMF also behaves differently at low-mass versus high-mass stars, with the low-mass stars ($M < 1\,\mathrm{M}_\odot$) following a lognormal behaviour while high-mass stars follow a power law with slope $\alpha = -2.35$. In all cases, we use broken power-law IMFs, defined piecewise with a break at $0.5\,\mathrm{M}_\odot$. *Non-universal IMF* (blue-shaded region): For masses $M < 0.5\,\mathrm{M}_\odot$, $\alpha = -1.3$ and for $M > 0.5\,\mathrm{M}_\odot$, α can take values in the range -1.8 to -2.35, shown here in the blue shaded region. *Benchmark canonical IMF* (purple solid curve): consists of a shallow power law like that in the Kroupa IMF at low masses and a Salpeter $\alpha = -2.3$ IMF at high masses. Throughout this paper, we will use this case as a benchmark against which to test the effects of allowing the IMF to vary.

variant of which was used in for example Baldry & Glazebrook 2003) and the Chabrier (2003) IMF which has a lognormal distribution for stars below approximately $1\,\mathrm{M}_\odot$ and a power law for stars greater than $1\,\mathrm{M}_\odot$. These two IMFs are plotted in Fig. 1. As long as a universal IMF is assumed, the high-mass behaviour of the IMF is approximately a power law with $\alpha = -2.35$, consistent with a Salpeter IMF (Baldry & Glazebrook 2003).[1]

However, while it is broadly accepted that a power-law Salpeter IMF does not hold true at low masses, questions regarding the range of environments over which the Salpeter power law is valid for stars with mass greater than $0.5\,\mathrm{M}_\odot$ remain significantly disputed. One of the most well-motivated regimes in which deviations from a Salpeter IMF at higher stellar masses could occur is the set of conditions in which Population III stars grow. For example, a top-heavy IMF at early times, which favours a higher average mass for Pop III stars, seems to be preferred by observations (Sharda & Krumholz 2021). One possible mechanism that could justify this behaviour is described in Sharda & Krumholz (2021), where a change in metallicity can shift the peak mass from approximately $0.5\,\mathrm{M}_\odot$ for solar metallicities to around $50\,\mathrm{M}_\odot$ at metallicities of Pop III stars. Furthermore, Pop III stars may exhibit energy production mechanisms inaccessible in Pop I and Pop II stars, as would be the case for Dark Stars (stars made of hydrogen and helium but powered by dark matter; Freese et al. 2016). In that case, it would be quite surprising if the IMF were to be consistent across all three populations.

In addition, there has been a growing body of evidence that seems to suggest that while the IMF behaves as a power law at high masses, the slope may depend substantially on environmental factors. Various authors identify multiple factors as possible sources of these deviations away from Salpeter. In addition to metallicity, these include: velocity dispersion (Ferreras et al. 2012; Ferré-Mateu et al. 2013), radius and surface mass density (La Barbera et al. 2019), and high turbulence (Chabrier, Hennebelle & Charlot 2014).

In this paper, we focus on a non-universal IMF that varies with the SFR of a star-forming region. Specifically, we explore a relationship that was identified in data from the spectroscopic GAMA survey (Driver et al. 2011), as analysed in Gunawardhana et al. (2011). The GAMA survey was undertaken by the Anglo-Australian telescope, which had measured the spectra of 120 000 galaxies at the time Gunawardhana et al. (2011) did their analysis. It has now taken the spectra of approximately 300 000 galaxies. The analysis in Gunawardhana et al. (2011) used the emission strength of the Hα line as a proxy to calculate the SFR of a galaxy, and then binned galaxies based on that SFR. Using a set of simulated galaxies, a power-law IMF was fit to the observed galaxies in each SFR bin, with the exponent α free to vary. Using these binned galaxies, they found a clear preference for a non-universal IMF, and that the variation could be described by the function, $\alpha_G \approx 0.36 \log\langle\mathrm{SFR}\rangle - 2.6$. Here, the average SFR, $\langle\mathrm{SFR}\rangle$, is measured in units of $\mathrm{M}_\odot\,\mathrm{yr}^{-1}$.

While this expression is the basis of the varying IMF we consider throughout the rest of this work, it is not in the most convenient form for our purposes. In particular, the independent quantity is the SFR, which is inferred from the luminosity of the Hα emission line. To calculate the astrophysical observables discussed below, we will need galaxy luminosity functions up to high redshifts. Unfortunately, the Hα emission line is not the ideal tracer of these luminosity functions as dust reprocesses most light emitted by galaxies into the infrared. On the other hand, galaxy surveys (and therefore galaxy luminosity functions) are more complete and readily available in the far-infrared (FIR) band (i.e. in the wavelength range 8–1000 μm) up to high redshifts. As a result, although using infrared luminosities can introduce significant uncertainty into the calculated SFRs (Madau & Dickinson 2014; Wilkins, Lovell & Stanway 2019), it is essential for our calculations below.[2] With this in mind, we convert $\langle\mathrm{SFR}\rangle$ to the

[1]Note that the typical break points for Kroupa and Chabrier are $0.5\,\mathrm{M}_\odot$ and $1\,\mathrm{M}_\odot$, respectively. Because the lognormal mass function smoothly turns over, they end up giving a similar distribution of stellar masses.

[2]Note that Wilkins et al. (2019) found that the precise stellar mass range considered can alter the FIR and Hα calibration factors, although the alteration is not necessarily the same between the two frequency bands. We therefore point out that by shifting from Hα to FIR, we are introducing additional error on the overall magnitude of each of the observables discussed below.

FIR luminosity $L_{\rm FIR}$, using fixed conversion factors from Kennicutt (1998).[3] This mimics the process used by Kennicutt (1998) in reverse, but implicitly assumes that the SFRs predicted by both tracers (Hα luminosity and FIR luminosity) are consistent. Using this procedure, we can rewrite the varying IMF expression from Kennicutt (1998) as

$$\alpha_{\rm var,>0.5} \approx 0.36 \log\langle L_{\rm FIR}\rangle - 6.1. \quad (3)$$

Ultimately, the IMF we consider here is empirically based, so we choose to confine ourselves to the range of IMFs that were observed in the corresponding data. In particular, the analysis in Gunawardhana et al. (2011) calculated IMFs ranging from $\alpha \approx -2.35$ to -1.8, with some populations of galaxies having IMFs as steep as $\alpha \approx -2.5$. We limit ourselves to consider only the range of $\alpha \in [-2.35, -1.8]$, which ensures that low luminosity galaxies have an IMF with slope $\alpha = -2.35$. [4] This α range corresponds to enforcing galaxies with a luminosity $\log\langle L/L_\odot\rangle \gtrsim 12$ to have $\alpha = -1.8$, and for galaxies with luminosity $\log\langle L/L_\odot\rangle \lesssim 10.4$ to have $\alpha = -2.35$. Furthermore, we explore only the effect of varying the IMF above a mass cutoff of 0.5 $M_\odot$, which gives comparable low-mass behaviour to the Chabrier and Kroupa IMFs. Below this mass cutoff, we use a fixed power law

$$\alpha_{\rm var,<0.5} = -1.3, \quad (4)$$

which matches the low-mass power law of the Kroupa IMF from 0.1 to 0.5 $M_\odot$.

We plot the range of IMFs that may appear in this luminosity-dependent varying IMF in Fig. 1 (blue band). Special attention is given to the IMF which consists of a shallow power law like that in the Kroupa IMF at low masses and a Salpeter IMF at high masses. Throughout this paper, we will use this *canonical* IMF (blue line) as a benchmark against which to test the effects of allowing the IMF to vary. One important fact that is readily seen from Fig. 1, and which has been noted by, for example Hopkins (2018), is that all of the IMF models we consider are quite similar, with only slight variation between them. However, despite the smallness of these variations, when the different IMF models are used to predict the values of observables, especially those that depend on integration of IMF-dependent quantities, we can see substantial differences appearing between the predictions made under those IMF models.

2.1 Luminosity to SFR calibration factor

We are interested in using observables which vary on cosmological scales to probe the IMF, and on those scales directly measuring the IMF is unrealistic. Instead, we will be using luminosity as a proxy for star formation, and by extension the IMF, as described in equation (3). Because all of the observables we consider are related to the rates at which stars form or die, a necessary factor in their calculation is the calibration factor, which we denote χ, that relates luminosity to SFR. In general, the calibration factor depends on the IMF, and because we are considering a non-universal IMF, we must consider how the χ will depend on our assumed IMF.

For a Salpeter IMF, multiple calculations of the calibration factor have been performed. In particular, Kennicutt (1998) found the calibration factor using three different wavelength ranges. While modelling of factors such as dust has improved (Kennicutt & Evans 2012), the values in Kennicutt (1998) are often useful as a benchmark for illustrative purposes. Throughout this paper, we focus on the FIR wavelength range, 8–1000 μm, for which the value of the calibration factor from Kennicutt (1998), assuming a Salpeter IMF, is

$$\chi_{\rm K98,FIR} = 4.5 \times 10^{-44}\, M_\odot\, {\rm yr}^{-1}\, {\rm s\, erg}^{-1}. \quad (5)$$

While the values obtained in Kennicutt (1998) are derived assuming a Salpeter IMF, and are reasonably consistent with our canonical IMF (as shown in Fig. 1), we are interested in IMFs with a range of high-mass behaviours. In order to calculate the impact that changing the IMF has on the calibration factor, we use the code PÉGASE.3 (Fioc & Rocca-Volmerange 2019), which simulates the radiation spectrum of a galaxy with a set of user-defined inputs (our particular scenarios are provided here: PÉGASE inputs). In each PÉGASE simulation, a cloud of gas is converted to stars at a prescribed SFR, and with a prescribed IMF. The stellar spectrum of each star that is formed is computed and allowed to evolve according to stellar evolution processes. These stellar spectra are then summed for the ensemble of stars in the galaxy at each time-step in the simulation, resulting in a galactic spectrum. That galactic spectrum is then adjusted to account for the reprocessing of stellar light by dust. Through this process, we can get a spectrum which may be integrated over various frequency ranges and used to calculate luminosities in different frequency bands.

In our simulations, we consider galaxies in the local universe that have a constant rate of star formation, and with other properties that we allow to vary. Besides allowing for different IMFs, we look at galaxies with two different geometries: discy spiral galaxies and spheroidal starburst galaxies, and with different metallicities and different dust models. In particular, for metallicity we consider a high-metallicity case with $Z = 0.026$ and a low-metallicity case with $Z = 0.013$.[5] For the dust models, we consider the dust models of Zubko, Dwek & Arendt (2004; ZWD), Li & Draine (2001), and Weingartner & Draine (2001; LWD). We summarize the combinations of the models we used in Table 1.

For each of the simulated galaxies, we calculate the luminosity in an 8–1000 μm wavelength band at different times from 10 Myr to 1 Gyr after the star formation begins. Fig. 2 shows how the calibration factor is affected considering each of these changes in input parameters. Here, it can be clearly seen that while changing the metallicity and dust model does lead to a distinguishable difference in the calibration factor, those differences are small compared to the changes induced by changing the IMF and geometry.

The convention for reporting a single calibration factor is to take the value at 100 Myr after the start of star formation. For other tracers

Table 1. Choices of input parameters in PÉGASE.3. We use the various scenarios to estimate the impact of these parameters on the luminosity to SFR calibration factor. For all other results in the paper, we use the calibration factors derived with the 'low Z' conditions.

Scenario	Z	Grains file
Low Z	0.013	ZDA
High Z	0.026	ZDA
Dust ZDA	0.0195	ZDA
Dust LWD	0.0195	LWD

[3]Specifically, we used the relation SFR $(M_\odot\, {\rm yr}^{-1}) = 4.5 \times 10^{-44} L_{\rm FIR}$ (erg s^{-1})(Kennicutt 1998). We discuss how this value depends on the IMF in Section 2.1.

[4]We note, however, that increasing the range of possible α's does not significantly affect our results. In particular, we verified that extending the range to $\alpha \in [-2.5, -1.8]$ has no noticeable effect on all results shown below.

[5]Note that some work has been done to self-consistently model metallicity evolution together with a varying IMF (Kobayashi 2010).

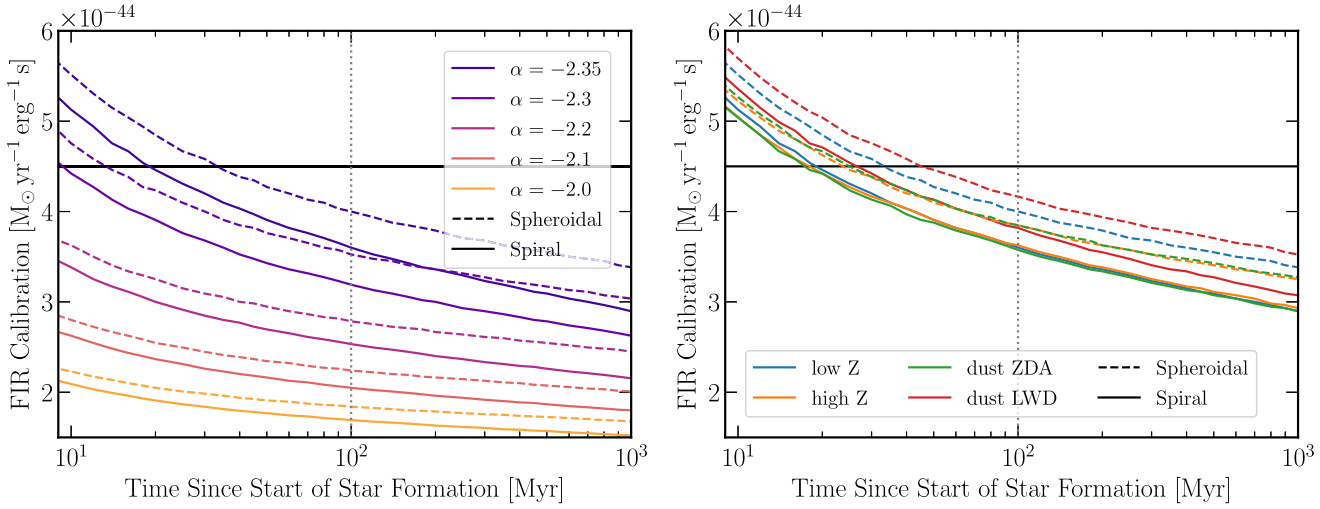

Figure 2. Calibration factor versus IMF slope: *(Left-hand panel)* Comparison of the calibration factor $\chi = R_{\rm SF}/L$ for a range of IMF slopes ($\alpha = -2.35$ to -1.8) used in our PÉGASE.3 simulations. We also show the impact of galaxy morphology by comparing calibration factors assuming spiral galaxies (solid lines) and spheroidal galaxies (dashed lines). The horizontal black line is the calibration factor identified in Kennicutt 1998 (Kennicutt 1998) for an IMF slope $\alpha = -2.35$ and assuming a spheroidal galaxy. Conventionally, the calibration factor is reported at 100 Myr following an onset of star formation, indicated here by a grey dotted vertical line. *(Right-hand panel)* The effect of different dust models and metallicities on the calibration factor, for both spiral and spheroidal morphologies with an IMF slope $\alpha = -2.35$. For comparison, all curves in the left-hand panel use the 'low Z' scenario.

of star formation, particularly ultraviolet luminosity, the calibration factor is effectively a constant after 100 Myr (Kennicutt 1998). While that is not the case for the FIR calibration factor, we adopt the same convention. Under this definition, we observe that the calibration factor we calculate for our canonical IMF and a spheroidal starburst galaxy is within 10 per cent of the calibration factor determined by Kennicutt (Kennicutt 1998) for a Salpeter IMF in a spheroidal galaxy. We do not account for other effects, e.g. stellar rotation on the calibrations (Horiuchi et al. 2013). Note that for $\alpha = -2.35$ we compared PÉGASE with STARBURST 99 (Leitherer et al. 1999) and found similar calibration factors.

3 PROBES OF A NON-UNIVERSAL IMF

Now that we have established our IMF models and the associated calibration factors, we will explore five astrophysical observables that intrinsically depend on the IMF. For each, we present the theoretical prediction for both IMF models and discuss whether current or future data are able to distinguish between the two.

3.1 Star formation rate density

We first explore how the SFR of galaxies could provide constraints on the nature of the IMF. The SFR is the rate at which gas in a star-forming region turns into stars, typically measured in $\mathrm{M_\odot\ yr^{-1}}$. While an interesting quantity in its own right, we will focus on the related SFRD, which measures the SFR per unit volume and typically has units $\mathrm{M_\odot\ yr^{-1}\ Mpc^{-3}}$. By looking at the SFRD rather than individual galaxies' SFR, we can average over the variance introduced because of different galactic properties and specifically explore how star formation depends on redshift. As a result, while both quantities give insight into the star formation process, the SFRD is more directly tied to the cosmic star formation history and less dependent on conditions within individual star-forming regions (Madau & Dickinson 2014).

While an understanding of the SFR is critical to theories of galactic evolution, it is challenging to measure directly. In fact, only in local systems, where stars can be resolved, can the SFR be directly measured (Kennicutt & Evans 2012; Calzetti 2013). Where young stars can be resolved, namely within the Milky Way and the nearest galaxies, it is possible to count those young stars and therefore directly estimate the SFR (Chomiuk & Povich 2011). In systems slightly more distant, where it is possible to resolve stars but impossible to see young stars shrouded in dust, fitting the galactic colour–magnitude diagram to simulations can provide an accurate measure of the SFR, among other properties. However, for more distant systems, in which stars cannot individually be resolved, an indirect measure of the SFR must be used, typically treating luminosity as a tracer of the SFR.[6] To convert from luminosity to SFR, one uses the calibration factor introduced in the previous section. As mentioned before, unfortunately these calibration factors are determined using simulations which require assumptions to be made about the IMF. In Section 2.1, we describe the impact that allowing the IMF to vary can have on the calibration factor.

To calculate the SFRD, we need the calibration factor as well as the luminosity distribution of galaxies. This distribution can be described through the luminosity function $\mathrm{d}N/\mathrm{d}\log L$,[7] which will generically be a function of redshift z. In all of our calculations, we use the set of luminosity functions calculated from data collected by the Herschel observatory in multiple complementary surveys including the PACS Evolutionary Probe (PEP), Herschel Multi-Tiered Extragalactic Survey (HerMES), and Herschel Great Observatories Origin Deep Survey (GOODS; Gruppioni et al. 2013). By including deep, pencil beam surveys like GOODS, these data include galaxies out to a redshift of $z \sim 4$. Meanwhile, broad, shallow surveys, like those in PEP and HerMES, can help provide more

[6]While the methods described here are among the most direct ways to estimate the SFR, work has been done to improve these estimates by combining these methods with observations that depend indirectly on the SFR. For example, see Wilkins, Trentham & Hopkins (2008a) and Wilkins et al. (2008b)

[7]Note that all equations below are written for a generic luminosity L. For notational simplicity, we therefore drop the subscript FIR on all luminosities. However, all calculations are performed within the FIR luminosity range (8–1000 μm).

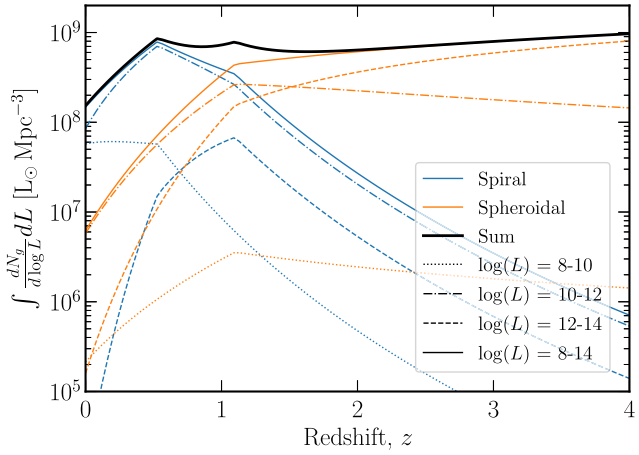

Figure 3. Luminosity density: We show how the luminosity functions $\mathrm{d}N_g/\mathrm{d}\log L$ from Gruppioni et al. (2013) depend on redshift. These luminosity functions give the density of galaxies as a function of luminosity and redshift. Here, we present the integral $\int \mathrm{d}L\ \mathrm{d}N_g/\mathrm{d}\log L$ for spiral and starburst galaxies. We also show the contribution to these integrals for the luminosity ranges: $10^8 - 10^{10} L_\odot$, $10^{10} - 10^{12} L_\odot$, and $10^{12} - 10^{14} L_\odot$. The luminosity functions in Gruppioni et al. (2013) are defined by fitting to modified Schecter functions, with parameters that are defined piecewise on z. These piecewise fits have breaks at the redshifts $z = 0.5$ and $z = 1.1$, so it is at these redshifts that we see peaks in observables like the SFRD.

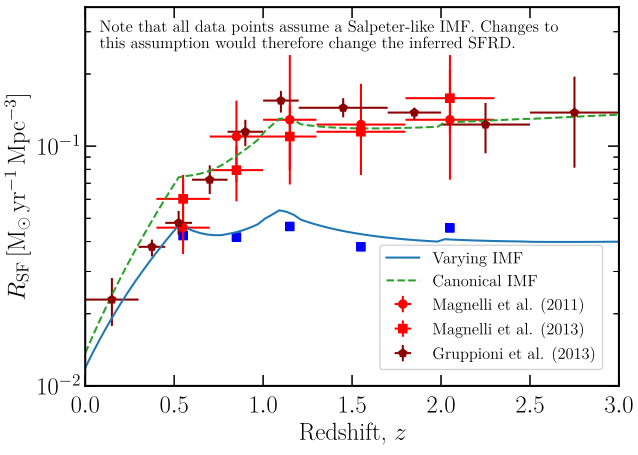

Figure 4. Star formation rate density: We compare the SFRD assuming a canonical IMF (green dashed curve) and a varying IMF (blue solid curve) to observational data as a function of redshift. The data were chosen to match with the FIR band we explore in this work. To limit clutter in the plot, we chose a representative subset from the catalogue of data (Madau & Dickinson 2014). Features in the prediction curves at $z = 0.5$, $z = 1.1$ arise from non-smooth features in the luminosity functions we consider, and features at $z = 1.0$, $z = 1.2$, and $z = 2.0$ arise from a non-smooth division of galaxies with an AGN into spiral and spheroidal sub-categories. While the observed data (red coloured points) agree quite well with the SFRD predicted from the canonical IMF, the data themselves are derived quantities which assume a Salpeter, Kroupa, or Chabrier IMF. For this reason, it is unsurprising that the observed data do not match the SFRD predicted using the varying IMF, particularly at high redshift. If a varying IMF is assumed when calculating the SFRD from observations, the results are expected to closely follow the predictions we make for a varying IMF. For illustration, we perform a preliminary reanalysis of the Magnelli et al. (2013) data using the luminosity functions described therein and the varying IMF we use in this work, depicted as blue points. This illustration is meant only to show proof of concept, and a more careful reanalysis should be performed, particularly in order to estimate uncertainties.

accurate identification of galaxies' morphologies. Therefore, from this combined data set, Gruppioni et al. (2013) were able to develop accurate, galaxy-morphology specific luminosity functions, labelled as 'spiral', 'starburst', and 'AGN-SF' for redshifts $z \approx 0 - 4$.[8] Respectively, these describe: spiral, discy galaxies without extreme star formation; spheroidal galaxies with intense star formation; and galaxies with a bright active galactic nucleus (AGN). We further distinguish the AGN category into spiral galaxies with an AGN and starburst galaxies with an AGN, based on the fraction of each type presented in Gruppioni et al. (2013). For both spiral galaxies with or without an AGN, we use the spiral calibration factors from the previous section. Similarly, for starburst galaxies with or without an AGN, we use the spheroidal calbiration factors.

In Fig. 3, we show the luminosity density as functions of redshift. In particular, we show the quantity $\int \mathrm{d}L\ \mathrm{d}N/\mathrm{d}\log L$for both spiral and spheroidal galaxies, as well as their sum. Assuming a canonical IMF, the calibration factor is constant, so this quantity is proportional to the SFRD, as can be seen clearly in equation (6). We additionally show the luminosity dependence of this integrated quantity by presenting contributions from three luminosity ranges. Comparing these contributions, we see that at low redshift the luminosity function is dominated by medium luminosity spiral galaxies while at higher redshifts, high luminosity spheroidal galaxies dominate. This shift in dominant contributors to the overall luminosity function causes distinct differences in observables, arising from the varying calibration factor. These differences appear in two ways. First, in our varying IMF model, the calibration factor is different for galaxies with different luminosities. Second, the calibration factor from spheroidal and spiral galaxies, even at the same luminosity, is slightly different. From the contributions in Fig. 3, we can therefore expect differences in any quantity derived from the calibration factor and luminosity functions at high and low redshift. In particular, based on where this turnover from spiral-dominated to spheroidal-dominated galaxies occurs, we should expect to see notable differences between the varying and canonical IMFs at redshifts of $z \gtrsim 0.5 - 1.5$.

From the calibration factor and luminosity function, we can calculate the SFRD for a given galaxy morphology g by integrating over the luminosity L:

$$R_{\mathrm{SF,\,g}} = \int \chi(L) L \frac{\mathrm{d}N_g}{\mathrm{d}\log L} \mathrm{d}\log L. \tag{6}$$

The total observed SFRD is then given by the sum over galaxy types $\sum_g R_{\mathrm{SF,\,g}}$, where $R_{\mathrm{SF,\,g}}$ is the SFRD contribution from galaxies of type g.[9] In Fig. 4, we compare the SFRD calculated using the varying IMF and canonical IMF. We also plot existing estimates of the SFRD, with data drawn from Magnelli et al. (2011, 2013) and Gruppioni et al. (2013). Note that we only show data that explicitly use the same FIR range as we consider for our luminosity functions. In principle, there is a wealth of other data from different wavelengths to compare

[8]Note that care must be taken in how AGNs are considered. The luminosity functions we consider are derived from the total luminosity of the galaxies, which includes both AGN and stellar sources. However, when calculating calibration factors, it is conventional to include only luminosity from stellar sources, not including AGN. As a result, introducing AGNs may decrease the calibration factors from what we derive in the previous section, but we do not consider the effects of such a decrease in this work.

[9]For simplicity, for the rest of this paper we drop the subscript g notation. All observable quantities defined below implicitly sum over galaxy type.

to e.g. Abdollahi et al. (2018), Madau & Dickinson (2014), Driver et al. (2018), Hopkins & Beacom (2006), and Fardal et al. (2007). We leave a more careful comparison to these data sets to future work.

At low redshift ($z \lesssim 0.15$), the SFRD calculated using a varying IMF is slightly lower than (within about 20 per cent of) the SFRD calculated using a canonical IMF and is consistent with observations. The primary reason for this behaviour is that at low redshifts, the dominant contribution to the luminosity functions comes from spiral galaxies with intrinsically lower galactic luminosity, which favour an IMF power law of $\alpha \approx -2.35$. At higher redshifts, the luminosity is dominated by a smaller density of intrinsically more luminous starburst galaxies, which favour a shallower IMF. Accordingly, we see that at redshifts $z \gtrsim 2$, the SFRD calculated using a varying IMF is up to a factor of three lower than the SFRD calculated from the canonical IMF and the reported observational data. However, all of the data plotted in Fig. 4, which is illustrative of much of the data in the literature (e.g. Hopkins & Beacom 2006; Fardal et al. 2007; Madau & Dickinson 2014; Abdollahi et al. 2018; Driver et al. 2018), assume an IMF with Salpeter-like behaviour at high stellar mass. In particular, in each of the three observed data sets shown here, the SFRD was calculated while assuming either a Chabrier IMF, a Kroupa IMF, or a pure Salpeter IMF. It is unsurprising then that the data so closely match the canonical IMF, while disagreeing with results obtained using univeral IMFs. [10] We therefore expect that reanalysing the SFR observations with a varying IMF would result in an SFRD that is lower than the existing data and that matches our predictions. We leave this analysis to future work. Since the effect of a varying IMF is significant, we also note that if the high-redshift SFR can be observed directly without relying on assumptions about the IMF, those observations could provide a useful probe of the IMF variability as a function of galaxy type.

3.2 Extragalactic background light

In addition to measuring the SFRD directly, we can also look at the EBL to potentially probe the IMF. The EBL is the integrated light from all sources in a particular direction. In particular, it includes light from all galaxies, even those too faint to resolve, and therefore provides an accurate measure of the luminosity function. In fact, the total EBL can be calculated as

$$L_{\mathrm{EBL,total}} = \int L \frac{\mathrm{d}n_g}{\mathrm{d}L}\mathrm{d}L = \int \frac{\mathrm{d}n_g}{\mathrm{d}\log L}\mathrm{d}L. \tag{7}$$

That is, the total EBL is simply an integral of the luminosity function over galaxy luminosities. Starting from the luminosity functions then, we can calculate the total EBL without introducing a dependence on the IMF, and so it is impossible to probe the IMF from the total EBL.

However, while the total EBL may be independent of IMF, the IMF affects the distribution of stellar masses. Because stars of different masses have different temperatures, and therefore different spectra, it is possible that the EBL spectrum may provide a way to probe the IMF. With this in mind, we followed the procedure outlined in Razzaque, Dermer & Finke (2009) to calculate an estimate of the EBL flux in the wavelength range 0.1–100 μm. Specifically, we calculate the spectrum of a star of given mass M with the corresponding effective temperature $T(M)$ as a blackbody spectrum $I_{\nu,BB}(T(M))$. We additionally denote the number of stars of a given mass inside of a galaxy as $\mathcal{N}(M, L)$. This number therefore intrinsically depends on the IMF. The EBL at a given frequency can then be calculated as

$$I_{\mathrm{EBL},\nu} = \int\int I_{\nu,BB}(T(M))\mathcal{N}(M, L)\mathrm{d}M \frac{\mathrm{d}N}{\mathrm{d}\log L}\mathrm{d}L. \tag{8}$$

Although this technique can give an estimate of the EBL emitted from galaxies, it does not take into account dust, and because of this offers only limited insight into the observed EBL. Absorption of starlight by dust causes the short-wavelength end of the spectrum to be reduced, while re-emission by that dust causes the long-wavelength end to be increased. While this generic picture is true in all dust models, exactly how dust affects the shape of the spectrum depends heavily on the dust model. We leave careful accounting of these dust effects to future work. Instead, we can look at the narrow range of frequencies where the effects from both dust absorption and emission on the EBL are minimized. In particular, we consider the range approximately 4–7 μm (Cardelli, Clayton & Mathis 1989; Kennedy et al. 2013). As can be seen in Fig. 5, in this wavelength range, the EBL predicted from both the canonical and varying IMF are quite similar, with the varying IMF prediction being very slightly bluer than the canonical prediction, and both visually fit existing data equally well.

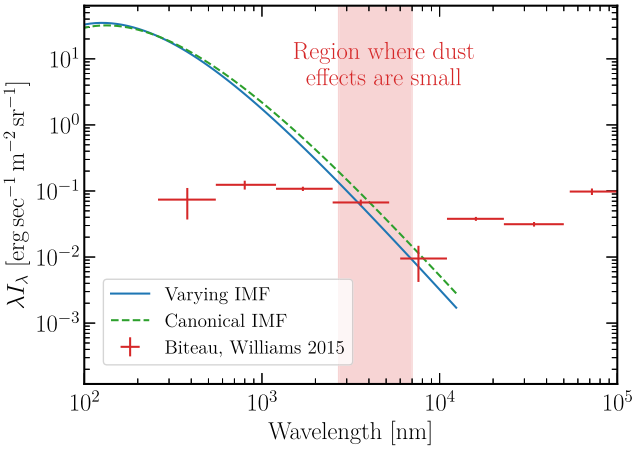

Figure 5. Extragalactic background light spectrum: Estimates of the EBL spectra assuming a varying IMF (blue solid curve), and a canonical universal IMF (green dashed curve). These are compared to data from Biteau & Williams (2015), showing the best-fitting values of the EBL calculated from various observed measurements of upper and lower bounds on the EBL spectrum. The estimates we show do not include processing from dust, so we generally expect the estimates to overpredict the intensity at short wavelengths, but begin to match at longer wavelengths. At the longest wavelengths, radiation from dust, rather than from stellar sources, will dominate the observed spectrum, and our estimates will underpredict the data. This behaviour is seen in our predictions which, in the wavelength range 3–7 μm which is least affected by dust, agrees quite well with data, regardless of IMF considered.

3.3 Core-collapse supernova rate

Along with the SFRD and EBL, we can look at the rate at which stars collapse into supernovae as a way to constrain the IMF. Stars which begin their life with a mass between 8 and approximately 125 $M_\odot$ are expected to end their life as a CCSN (Heger et al. 2003). Standard CCSNe occur when their iron or oxygen-neon-magnesium core, produced through nuclear fusion, exceeds the Chandresekhar mass limit and rapidly collapses (Couch 2017; Janka 2017; Burrows & Vartanyan 2021). This facilitates electron capture

[10] Work using different non-universal IMFs, like (Chruślińska et al. 2020), shows a similar trend toward reduced SFRD at high redshifts, but by a different factor.

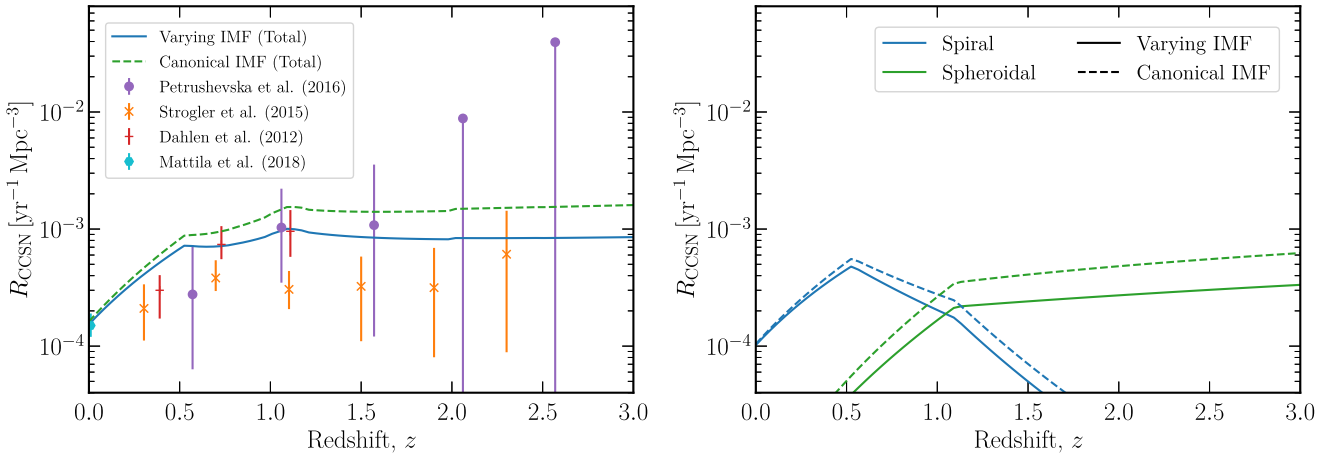

Figure 6. Core collapse supernova rate density: *(Left-hand panel)* Comparison of the predictions of the rate density of CCSNe assuming either a canonical IMF (green dashed curve) or a varying IMF (blue solid curve) with observational data as a function of redshift. See Fig. 4 for discussion of features at $z = 0.5$, $z = 1.0$, $z = 1.1$, $z = 1.2$, and $z = 2.0$. *(Right-hand panel)* Rate of supernovae in each of the galaxy morphologies we consider. Here, blue corresponds to spiral galaxies, while green corresponds to spheroidal starburst galaxies. Again, dashed lines correspond to the canonical IMF, while solid lines correspond to the varying IMF.

on nuclei and free protons in the centre of the collapsing core, which makes matter more neutron rich and produces a copious number of electron neutrinos (Bethe et al. 1979a; Fuller 1982). Once the density reaches the nuclear saturation density (approximately 2.6×10^{14} g cm^{-3}; Bethe et al. 1979a), the strong nuclear force stops the collapse of the inner core (Bethe et al. 1979a; Couch 2017; Branch & Wheeler 2017). The sudden halt causes the core to bounce and launches a shock wave, which carries stellar material away from the core. The shock stalls after losing energy through the dissociation of heavy nuclei but can be re-energized by neutrinos, which revive the shock leading to a successful explosion. This is the so-called neutrino-driven delayed explosion mechanism (Colgate & White 1966; Bethe & Wilson 1985).

Eventually, the electromagnetic radiation emitted by the material ejected in a successful explosion is observed as a supernova. Depending on the chemical makeup of the ejected material, CCSNe are classified as Type Ib, Ic, or II supernovae (Turatto 2003; Smith 2014). The supernova can leave behind either a neutron star or black hole depending on how much energy is imparted to the shock wave by neutrinos, compared to the gravitational binding energy of the outer layers of the star. Because some of these types of supernovae will be more detectable than others and any stars that collapse directly to a black hole do not produce a supernova, the fraction of core collapses that can be observed through electromagnetic signatures will depend on the fate of the collapsing massive star, and that in turn may depend on the IMF.

As with the SFR, we will again focus on the core-collapse supernova rate density (CCSNRD), which allows us to focus on only the redshift dependence. On time-scales that are long compared to the lifetime of a star massive enough to undergo core collapse ($\lesssim 10$ Myr), we can assume that when one star goes supernova another star of equal mass is formed. As a result, we can calculate the CCSNRD directly from the SFRD of stars with mass greater than approximately 8 M$_\odot$. In particular,

$$R_{\rm CCSN}(z) = \int \chi(L) L \frac{{\rm d}N}{{\rm d}\log L} \frac{\int_{8{\rm M}_\odot}^{M_{\rm max}} \xi(M){\rm d}M}{\int_{M_{\rm min}}^{M_{\rm max}} M\xi(M){\rm d}M} {\rm d}\log L. \quad (9)$$

Here, $M_{\rm min}$ and $M_{\rm max}$ refer to the minimum and maximum masses stars can take in the IMF we consider. In all of our calculations, we use $M_{\rm min} = 0.1\,{\rm M}_\odot$ and $M_{\rm max} = 125\,{\rm M}_\odot$, respectively, the approximate lowest mass at which stars can fuse hydrogen and a somewhat arbitrary high-mass cutoff that does not significantly affect our results. The factor of M in the denominator is necessary because SFRs measure the total mass of stars that form, whereas the core-collapse rate measures the number of supernova events.

In Fig. 6, we compare the CCSNRD we predict from a varying IMF to that predicted from a canonical IMF and to observed CCSNRD data from Petrushevska et al. (2016), Strolger et al. (2015), Dahlen et al. (2012), and Mattila et al. (2012). As in the case of SFRs, at low redshift, all three CCSNRD are consistent. At high redshift, the CCSNRD predicted using the varying IMF is slightly lower than that predicted using the canonical IMF, but the discrepancy between the CCSNRD is significantly smaller than the related difference between SFRs. This improved agreement is to be expected because the SFR's dependence on the IMF partially cancels against the explicit IMF dependence in equation (9), as discussed in Madau & Dickinson (2014). Ultimately, the existing CCSNe data appear to agree with either IMF model equally well. However, as new observatories including, the *James Webb Space Telescope* (Regős & Vinkó 2019), the Vera Rubin Observatory (through the LSST survey; Ivezić et al. 2019), *Euclid* (Laureijs et al. 2011), and the *Nancy Grace Roman Telescope* (Koekemoer et al. 2019) begin to take data, estimates of the high redshift CCSNRD will become more precise, potentially favouring one model over the other. Likewise, gravitational wave detectors may offer another avenue to probe the supernova rate, and consequently the SFR, by measuring the binary black hole (BBH) merger rate (Vitale et al. 2019). However, it should be noted that the binary merger rate would preferentially reflect the supernova rate in low-metallicity environments and would be subject to the same sorts of uncertainties as SNeIa (see below), which could make distinguishing between the two IMF models more challenging.

We find that the two IMF models produce an $\mathcal{O}(2)$ difference in the total CCSN rate at redshifts greater than approximately 1.5. Therefore, at least a 100 per cent determination of the SN rate for $z > 1.5$ will be required to distinguish these two scenarios. Based on projections of the rates of supernovae expected to be observed by the *Roman Telescope* (Rose et al. 2021), it is not unreasonable to expect observational uncertainties at that level. Furthermore, a greater difference in the predicted supernova rates under our two models may appear if changing the IMF changes the fraction of stars that collapse into black holes versus those that collapse to neutron

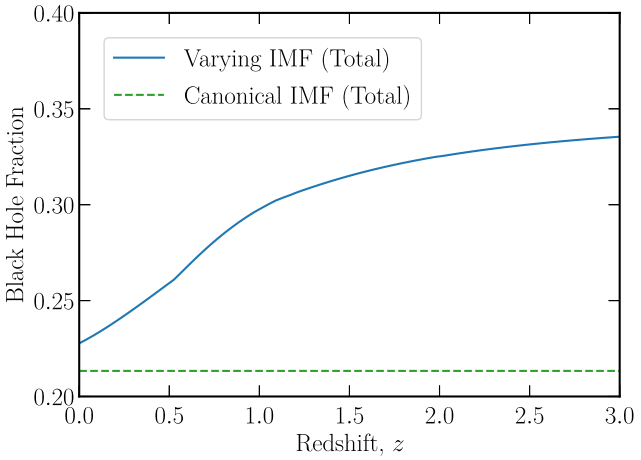

Figure 7. Fraction of black hole forming collapses: The fraction of supernovae that result in black holes, rather than neutron stars. For the canonical IMF, approximately 21 per cent of stellar collapses lead to black hole formation (this fraction is assumed to be constant as a function of the redshift for simplicity), while for the varying IMF, this fraction depends on redshift, reaching approximately 35 per cent at $z = 3$.

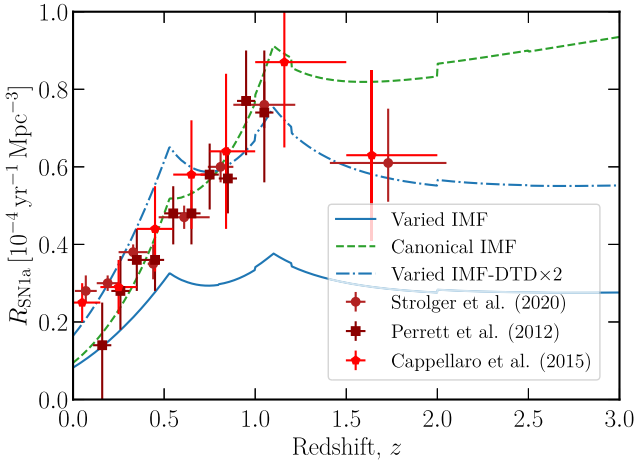

Figure 8. Type Ia supernova rate density: We compare the rate density of SNeIa, assuming either a canonical IMF (green dashed) or varying IMF as described in the text (blue), to a selection of observed data. See Fig. 4 for discussion of features at $z = 0.5$, $z = 1.0$, $z = 1.1$, $z = 1.2$, and $z = 2.0$. Predictions of the supernova rate depend on a poorly constrained delay time distribution, and by increasing the overall normalization of this DTD by a factor of 2 (still within 1σ uncertainties), we can increase the varying IMF result from the blue solid curve to the blue dot–dashed curve.

stars. All else held equal, a shallower IMF would increase the fraction of stars that evolve to black holes and decrease the fraction that evolve to neutron stars, relative to a steeper IMF. As shown in Fig. 7, this is precisely the situation we expect from the varying versus canonical IMF. As a result, we can expect that a varying IMF would lead to fewer observable CCSNe than the canonical IMF, particularly at high redshifts, all other factors held equal.

3.4 Type Ia supernova rate

As with CCSNe, we can hope to probe properties of the IMF by looking at SNeIa. Type Ia supernovae occur when mass accretes on to white dwarfs from a giant star, typically when the two form a binary (Mazzali et al. 2007). As the mass of the white dwarf approaches the Chandrasekhar mass (Chandrasekhar 1931), temperatures and densities within the core of the star become high enough to initiate nuclear reactions from the abundant carbon and oxygen. These nuclear reactions produce so much energy that the entire star becomes unbound. Nuclear decays within the ejected material can then be observed as a SNeIa.

For our purposes, SNeIa can be seen as a tracer of SFR like the CCSN rate. In addition, measurements of the SNIa rate do not require one to use a calibration factor and are therefore relatively independent of the IMF. However, since SNeIa are sourced by white dwarfs, which form from stars whose lifetimes are of the order of 1–10 Gyr, they can only occur after enough time has passed for the white dwarf to accrete sufficient mass. Both the lifetime of the progenitor star and the period between the formation of a white dwarf and the occurrence of an SNIa must be accounted for when calculating the SNIa rate. This accounting is done through a delay-time distribution (DTD) $F(\tau)$, which measures the probability that a star formed at some time $t - \tau$ will undergo SNIa at time t. Note that by defining the DTD in this way, we implicitly incorporate the fraction of white dwarfs that exist in binaries and can undergo SNIa into the DTD. In our calculations, we use the simple approximation that $F(\tau) \propto \tau^{-1}$, justified in Maoz, Mannucci & Nelemans (2014). The SNIa rate density can therefore be calculated from the convolution

$$R_{\rm SNIa} = \int_0^t R_{\rm SF}(t-\tau)F(\tau){\rm d}\tau. \quad (10)$$

Here, we convert between redshift and time assuming a flat ΛCDM Universe that is dominated by Λ and matter, and where $\Omega_{m,0} = 0.308$ (Ade et al. 2016).

In Fig. 8, we compare observed SNIa rates, using data from Strolger et al. (2020), Perrett et al. (2012), and Cappellaro et al. (2015), with predictions of the supernova rate assuming a canonical IMF and a varying IMF. To make this comparison, we fixed the normalization of the DTD to $10^{-3}\,{\rm M}_\odot^{-1}$ in order to match the DTD presented in Maoz et al. (2014).[11] Using this normalization, the canonical IMF is largely consistent with the data, while the varying IMF leads to an SNIa rate that is consistently smaller than the observed SNIa rate. However, if we allow the normalization of the DTD to vary, then increasing it by a factor of two produces much closer agreement between the varying IMF and observed SNIa rates. This change to the normalization is still within the 1σ confidence range for the DTD. In other words, based on current observations and their uncertainties, the varying IMF cannot be ruled out, and more precise measurements of the DTD would be necessary to place meaningful constraints on either IMF model.

3.5 Diffuse supernova neutrino background

Finally, in addition to directly observing of supernova rates, we can look to the neutrino supernovae produce in order to estimate their rate, and therefore potentially probe the IMF. Despite being relatively rare in any individual galaxy, supernovae are quite common throughout the Universe. Combining this with the fact that a single CCSN produces an immense number of neutrinos (approximately

[11] However, as noted in Maoz et al. (2014), measurements of the DTD in different environments (e.g. dwarf galaxies, galaxies, and galaxy clusters) can vary by an order of magnitude.

10^{58}; Mirizzi et al. 2016; Burrows & Vartanyan 2021) leads to the emergence of a background of neutrinos that is isotropic and nearly constant in time. This neutrino flux is commonly named the DSNB (Bisnovatyi-Kogan & Seidov 1984; Krauss, Glashow & Schramm 1984; Wilson et al. 1986; Beacom 2010; Lunardini 2016; Mirizzi et al. 2016).

Only in recent years have experiments begun to approach the sensitivity necessary to directly observe the DSNB (Malek et al. 2003; Bays et al. 2012; Zhang et al. 2015; Abe et al. 2022, 2021; Li, Vagins & Wurm 2022). While no signal has yet been detected, the enrichment of Super-Kamiokande (SK) with gadolinium (Beacom & Vagins 2004; Horiuchi, Beacom & Dwek 2009) and the future proposed and planned experiments such as Hyper-Kamiokande (HK), JUNO, Jinping, and THEIA (An et al. 2016; Beacom et al. 2017; Abe et al. 2018; Sawatzki, Wurm & Kresse 2021; Li et al. 2022) are expected to have enough sensitivity to make a first detection in the coming years. Once observed, the DSNB will provide a test of astrophysical observables (Lunardini 2009; Keehn & Lunardini 2012; Nakazato 2013; Nakazato et al. 2015; Priya & Lunardini 2017; Møller et al. 2018; Horiuchi et al. 2021; Kresse, Ertl & Janka 2021; Singh & Rentala 2021; Libanov & Sharofeev 2022), neutrino flavor physics (Lunardini & Tamborra 2012; Tabrizi & Horiuchi 2021; Suliga, Beacom & Tamborra 2022), and physics beyond the Standard Model (Ando 2003; Fogli et al. 2004; Goldberg, Perez & Sarcevic 2006; Baker et al. 2007; Farzan & Palomares-Ruiz 2014; Jeong et al. 2018; de Gouvêa et al. 2020, 2022; Creque-Sarbinowski, Hyde & Kamionkowski 2021; Das & Sen 2021; Suliga et al. 2022).

3.5.1 *Theoretical models*

The calculation of the DSNB flux requires two components: the rate of supernovae as a function of their progenitor masses and the time-integrated neutrino energy spectra associated with each supernova. The former can be calculated as described in Section 3.3, while a calculation of the latter is sketched here. Following Møller et al. (2018) and Ashida & Nakazato (2022), we consider three possible outcomes of supernovae, depending on the mass of their stellar progenitor. Stars can either evolve into black holes or low/high-mass neutron stars. A characteristic neutrino spectrum is then associated with each type of explosion. More details on these spectra can be found in Appendix A.

As discussed in Appendix A, the characteristic neutrino spectra associated with the different supernovae outcomes can be significantly different. The DSNB signal is therefore also affected by the fraction of black hole forming collapses (Lunardini 2009). Unfortunately, the fraction of stellar collapses leading to black hole formation is unknown. Recent theoretical work and observational surveys indicate that this fraction could be approximately 10–40 per cent of all CCSNe (Kochanek et al. 2008; Lien, Fields & Beacom 2010; Horiuchi et al. 2014; Gerke, Kochanek & Stanek 2015; Ertl et al. 2016; Sukhbold et al. 2016; Adams et al. 2017a, b; Davies & Beasor 2020; Neustadt et al. 2021; Byrne & Fraser 2022). For the canonical IMF, our DSNB modelling follows one of the scenarios considered in Møller et al. (2018) where the fraction of progenitors evolving into black holes is set to 21 per cent and for simplicity it is assumed to be constant as a function of redshift out to at least $z = 5$. To make this assumption, we implicitly assume that both the stellar masses that evolve to black holes and the IMF do not change over cosmological history. However, when we consider the varying IMF, we cannot assume that the IMF is constant as a function of redshift; in fact, because it depends explicitly on the SFR, which evolves over cosmic history, the varying IMF cannot remain constant. As a result, we expect to see a substantially larger fraction of stars evolve to black holes at high redshifts in the non-universal case than in the canonical case, as seen in Fig. 7.[12] In addition, because our main goal is to investigate the impact of the variable IMF on the DSNB, we do not include neutrino oscillations in our modelling, as they would change the DSNB in the same way in both cases, i.e. canonical and variable IMF.

Making use of the supernova rate and the neutrino spectrum, we can calculate the DSNB flux Φ as a function of neutrino energy E. Specifically,

$$\Phi(E) = c \int_0^{z_{\max}} \frac{\mathrm{d}z}{H(z)} \times \int \chi(L) L \frac{\mathrm{d}N}{\mathrm{d}\log L} \left[\int_{8M_\odot}^{M_{\max}} \frac{\mathrm{d}n}{\mathrm{d}E'} \frac{\xi(M)\mathrm{d}M}{\overline{M}} \right] \mathrm{d}\log L, \quad (11)$$

where $\frac{\mathrm{d}n}{\mathrm{d}E}$[13] is the neutrino spectrum, $E' = E(1+z)$ is the source energy necessary at a redshift of z to be observed with energy E, and $\overline{M} = \int_{M_{\min}}^{M_{\max}} M\xi(M)\mathrm{d}M$ is the average mass of newly formed stars. The integral $\int \chi(L) L \frac{\mathrm{d}N}{\mathrm{d}\log L} \mathrm{d}\log L$ is equivalent to R_{SF} if the term in brackets does not depend on luminosity. While this condition is met for the canonical IMF, when we consider a varying IMF, the IMF depends on luminosity, so the factor in brackets picks up a dependence on luminosity. In addition, $H(z) = H_0[\Omega_{m,0}(1+z)^3 + (1-\Omega_{m,0})]^{1/2}$ is the Hubble expansion parameter at z, where we assume a flat ΛCDM universe dominated by matter and Λ, with $\Omega_{m,0} = 0.308$ and $H_0 = 67.8\,\mathrm{km\,s^{-1}\,Mpc^{-1}}$ (Ade et al. 2016).

Using the CCSNRD calculated from both a canonical and varying IMF we find the DSNB fluxes shown in Fig. 9. We emphasize here that we have only considered a single benchmark for each IMF model, but in reality there are a number of other uncertainties which would create a band of possible DSNB realizations. We do not directly consider these uncertainties in the modelling of the DSNB (i.e. in Fig. 10), although below we account for a systematic uncertainty when evaluating the discriminability of the two IMF models. For reference, we also show a hatched region which shows the approximate parameter space currently ruled out by SK observations, as well as the primary signal region for SK and future detectors (El Hedri, Ashida & Giampaolo 2021). Perhaps the most notable result is the similarity between the predictions from using the canonical and varying IMFs, especially at energies greater than approximately 20 MeV. While this will likely make it difficult to distinguish between the two scenarios once the DSNB is detected, it clearly demonstrates that the DSNB is robust to significant changes to the IMF.

At lower energies (below approximately 20 MeV), we predict the DSNB flux to be slightly lower when assuming a varying IMF than when assuming a canonical IMF. While the IMFs we consider give similar predictions for the CCSNRD at low redshift, they begin to disagree at higher redshifts. The difference in the DSNB flux that we see here ultimately arises from this difference

[12]It should be noted that this fraction is calculated assuming that the stellar mass is the only factor which controls whether a supernova leads to a black hole formation or not (see Appendix A.). It is therefore constant for the canonical universal IMF. Other stellar properties, such as metallicity, may lead to changes in the fraction of supernovae that lead to black hole formation.
[13]Note that although equation (11) is true for all flavors, as mentioned in Appendix A we will focus solely on electron-antineutrinos since they have the best detection prospects.

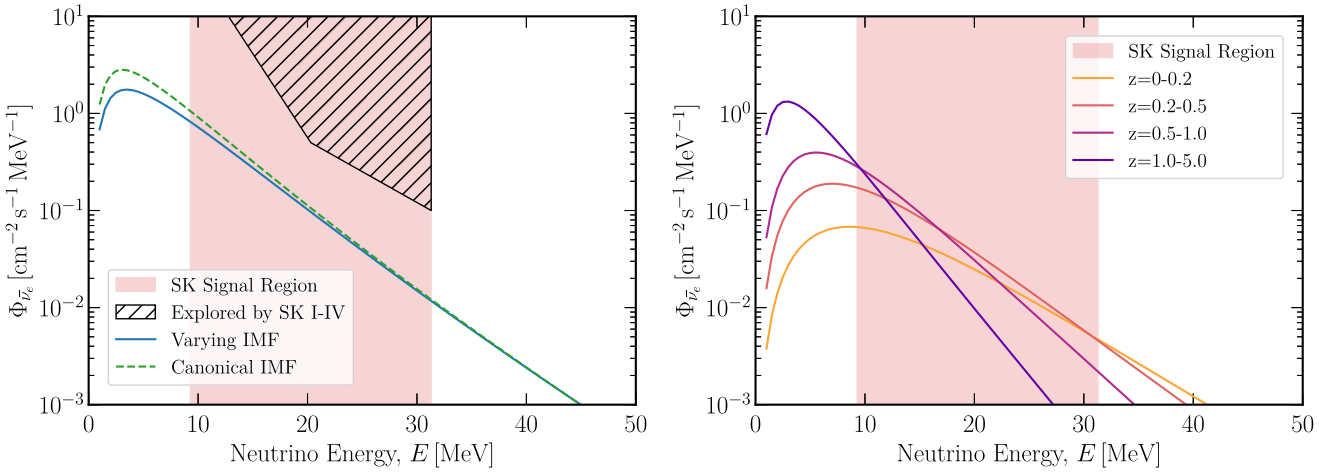

Figure 9. Diffuse supernova neutrino background flux: *(Left-hand panel)* We compare the predicted DSNB $\bar{\nu}_e$ flux, assuming either a canonical (green dashed) or varying IMF (blue solid) with the region probed by SK (hatched) (Abe et al. 2021). The red shaded region indicates the range of energies that could be observable by SK with the addition of gadolinium. The different IMFs might have an impact on the observed DSNB flux only at low energies, and it would be difficult to distinguish this difference against background neutrino sources. *(Right-hand panel)* We show the DSNB broken down into contributions from different redshift bins for the varying IMF. Because the emitted neutrinos are redshifted, distant supernovae only contribute significantly at low energies.

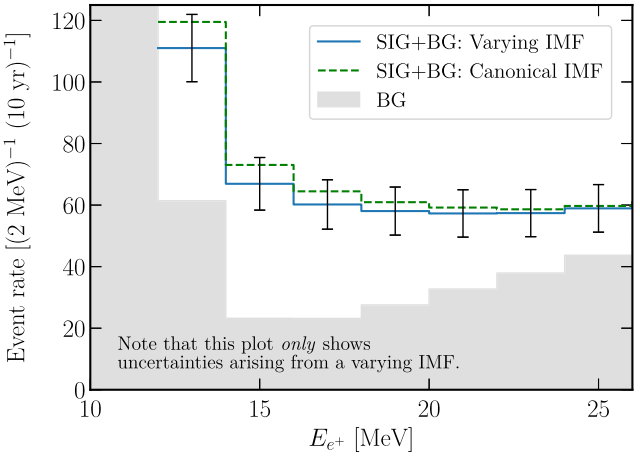

Figure 10. Diffuse supernova neutrino background rate: $\bar{\nu}_e$ DSNB event rates in HK enriched with gadolinium detectors for 10 yr of data taking. The sum of the $\bar{\nu}_e$ DSNB event rate plus background rate for the varying IMF (canonical) is plotted with solid blue (dashed green) line. The background rates are depicted as grey regions, and the error bars reflect the $\pm 1\sigma$ statistic uncertainties. As discussed in the main text, while SK cannot distinguish the two investigated IMF scenarios, HK might present a low significance hint towards a particular scenario. Note that we do not show other astrophysical uncertainties (e.g. errors on the SFR and uncertainty in the neutrino flux modelling), but partially account for this with a systematic uncertainty (see main text for details).

in supernova rates. This is only noticeable at low neutrino energies because distant supernovae only contribute significantly to the low-energy spectrum. At higher energies, because of the redshifting of the neutrinos as they propagate, the source energy $E' = E(1+z)$ can be significantly higher for distant supernovae than for nearby ones. As a result, the contribution to the DSNB flux from distant supernovae comes from a higher energy portion of the spectrum, which is exponentially suppressed. This effect is illustrated in the right-hand panel of Fig. 9 where we show the contribution to the DSNB in different redshift bins. Therefore, while a varying IMF is likely indistinguishable from the canonical IMF at high energies, sufficiently precise measurements of lower energy neutrinos may allow some degree of distinction between the two models.

Varying the IMF is not the only source of uncertainty expected to appear in the low-energy DSNB region (around 20 MeV). Variations to the star formation histories, for example, could yield comparable differences between DSNB predictions (Singh & Rentala 2021; Kresse et al. 2021), which will be degenerate with differences due to variations of the IMF. Furthermore, additional uncertainties in the DSNB flux which may appear, independent of the choice of IMF, include the unknown fraction of high-mass stars that evolve to black holes and the neutrino spectra emitted during this evolution (Lunardini 2009; Horiuchi et al. 2018; Kresse et al. 2021), the precise normalization of the CCSN rate (Horiuchi et al. 2011; Mathews et al. 2014), the evolution of neutrino flavours in the dense medium encountered during supernovae (Duan, Fuller & Qian 2010; Chakraborty et al. 2016; Tamborra & Shalgar 2021), and any possible stellar binary interactions (Horiuchi et al. 2021). To partially account for these uncertainties in subsection 3.5.2, we include a systematic uncertainty of 50 per cent in our calculations of the discriminating power of the detectors to the varying IMF.

3.5.2 Expected sensitivities of Super-Kamiokande and Hyper-Kamiokande

Although no detection of the DSNB has yet been made, the strongest constraints come from the SK experiment (Bays et al. 2012; Abe et al. 2021). In 2019, upgrades to SK began which allowed for the introduction of gadolinium into the SK tank by 2021. The gadolinium doping will make the detection of electron antineutrinos significantly easier, which will subsequently improve our ability to detect neutrinos from the DSNB (Beacom & Vagins 2004). As a result, it is expected that a positive measurement of the DSNB will be observed in the near future (Li et al. 2022).

Fig. 10 shows the predicted accumulated DSNB flux after 10 yr of operation of HK (3740 kton yr exposure) compared to its respective neutrino backgrounds, where we assume a concentration of 0.1 per cent $GdCl_3$ in water. The blue solid (green dashed) line depicts the combined neutrino flux from both the DSNB and background sources, where we calculate the DSNB flux using a varying IMF

(canonical IMF). Sources of background neutrinos that we consider include atmospheric charged-current events, invisible muons, ^{9}Li spallation, and reactor antineutrinos (Abe et al. 2018, 2021).

We can use a simple $\Delta\chi^2$ Pearson test to estimate the detection prospects of distinguishing between the varying IMF and canonical IMF. In both SK (225 kton yr exposure with 0.1 per cent $GdCl_3$) and HK, the two IMFs are not distinguishable at the 3σ level, even after 10 yr of data collection. Furthermore, in SK, the two models remain indistinguishable at the 1σ level. However, in HK, the varying and canonical IMFs are distinguishable at the 1.3σ level. This marks an upper bound to the distinguishability, as we have not introduced other sources of uncertainty. Including a systematic uncertainty for the background of 20 per cent and for the DSNB models of 50 per cent reduces the difference between the two models to 1.1σ (note that these additional systematics are not shown in Fig. 10). Once SK or HK detects the DSNB, it may be possible to generate an improved statistic, using an unbinned maximum likelihood ratio test with a parametrized family of models that include the canonical and varying IMFs, which could allow for a better ability to distinguish between these two models, assuming all other uncertainties become negligible in comparison.

4 CONCLUSION AND OUTLOOK

In this paper, we explored whether one can find evidence for a non-universal IMF in five astrophysical observables that arise from integrating over cosmological scales. Throughout, we have seen that these observables show small but non-zero differences when assuming the non-universal IMF (described in Section 2) versus a canonical universal IMF. The differences are typically too small to distinguish in currently existing data, but as detectors improve, there are a variety of signals which may offer practical ways to study the IMF. In particular, we find that studying the SFR and the core-collapse rate at high redshifts ($z \gtrsim 0.5$) may offer the greatest distinguishability between the different IMF models.

At redshifts greater than approximately 0.5, the SFR predicted assuming a varying IMF is lower than the corresponding prediction from a canonical IMF by up to a factor of ~ 3 (see Fig. 4). Because observing the SFR requires a calculation that depends strongly on the assumed IMF, the predictions, though significantly different, can both still be consistent with current observations. However, due to the SFR's prominent role in, for example, modelling star formation histories and cosmological simulations, it would be interesting to see whether an indirect test of the SFR could favour one IMF model over the other. For example, the BBH merger rate (Fishbach, Holz & Farr 2018; van Son et al. 2022) acts as an independent probe of the core collapse rate. LIGO and Virgo, at design sensitivity, are expected to observe BBH mergers up to redshifts of around one. On the other hand, 3rd generation telescopes may reach $z \sim 15$ and thus independently measure the SFRD to a few per cent according to Vitale et al. (2019). We leave a more careful examination of this method to future work.

Similarly to the SFR, above $z \gtrsim 0.5$ the core-collapse rate can differ by a factor of ~ 2 between the two IMF models (see Fig. 6). Current observations of core-collapse rates are still too poor at high redshifts to distinguish between these models. However, next-generation telescopes such as *James Webb Space Telescope* (Regős & Vinkó 2019), *Roman Space Telescope* (Koekemoer et al. 2019), *Vera Rubin Telescope* (through the LSST; Ivezić et al. 2019), and *EUCLID* (Laureijs et al. 2011), may provide significantly better rate estimates at these high redshifts. An additional subtlety here is that a varying IMF will produce a larger fraction of black hole collapses (see Fig. 7) which may be less luminous. A careful treatment of the observational efficiency of any core-collapse rate measurement is therefore required to distinguish the two IMF models.

The stellar IMF plays a fundamental role throughout astrophysics and many unsolved questions require an accurate model of the IMF to address. It is therefore vital that new methods are developed to decipher its dependence on the local environment. Here, we have examined a few indirect methods. Future work should more carefully examine the most promising of these scenarios with a meticulous treatment of their associated uncertainties, including studying whether the impact of different IMFs can be distinguished from potentially degenerate or partially degenerate sources of uncertainty. Moreover, combining the different probes presented here may lead to significantly tighter constraints on possible IMF variations. Through this, we hope that indirect probes may provide additional evidence towards distinguishing a varying IMF.

ACKNOWLEDGEMENTS

We thank Andrew Hopkins for a careful reading of the manuscript and helpful discussions. TE and KF acknowledge support by the Vetenskapsrådet (Swedish Research Council) through contract No. 638-2013-8993 and the Oskar Klein Centre for Cosmoparticle Physics at Stockholm University. TE was supported by the NWO (Dutch Research Council) through the VIDI research program 'Probing the Genesis of Dark Matter' (680-47-5). JZ and KF are grateful for support from the Jeff & Gail Kodosky Endowed Chair held by KF at the University of Texas. JZ and KF acknowledge funding from the U.S. Department of Energy, Office of Science, Office of High Energy Physics program under Award Number DE-SC0022021. AMS acknowledges the support form the US National Science Foundation (Grant No. PHY-2020275). In Copenhagen, this work was supported by the Villum Foundation (Projects Nos. 13164 and 37358), the Danmarks Frie Forskningsfonds (Project No. 8049-00038B), the Deutsche Forschungsgemeinschaft through Sonder- forschungbereich SFB 1258 'Neutrinos and Dark Matter in Astro- and Particle Physics' (NDM). The work of SH is supported by the U.S. Department of Energy under the award number DE-SC0020262, NSF grant numbers AST-1908960 and PHY-1914409, and JSPS (Japan Society for the Promotion of Science) KAKENHI grant number JP22K03630. SA was supported by MEXT (Japanese Ministry of Education, Culture, Sports, Science, and Technology) KAKENHI grant numbers JP20H05850 and JP20H05861. This work was supported by World Premier International Research Center Initiative (WPI Initiative), MEXT, Japan. AMS and SH would like to thank Kavli Institute for Theoretical Physics for the hospitality during this work. This research was supported in part by the National Science Foundation under grant no. NSF PHY-1748958.

DATA AVAILABILITY

The data underlying this article are available in a Github repository at https://dx.doi.org/10.5281/zenodo.6626203.

REFERENCES

Abdollahi S. et al., 2018, Science, 362, 1031
Abe K. et al., 2018, preprint (arXiv:1805.04163)
Abe K. et al., 2021, Phys. Rev. D, 104, 122002
Abe S. et al., 2022, ApJ, 925, 14
Adams S., Kochanek C., Gerke J., Stanek K., Dai X., 2017a, MNRAS, 468, 4968

Adams S., Kochanek C., Gerke J., Stanek K., 2017b, MNRAS, 469, 1445
Ade P. A. R. et al., 2016, A&A, 594, A13
An F. et al., 2016, J. Phys. G: Nucl. Phys., 43, 030401
Ando S., 2003, Phys. Lett. B, 570, 11
Ashida Y., Nakazato K., 2022, ApJ, 937, 30
Baker J., Goldberg H., Perez G., Sarcevic I., 2007, Phys. Rev. D, 76, 063004
Baldry I. K., Glazebrook K., 2003, ApJ, 593, 258
Bays K. et al., 2012, Phys. Rev. D, 85, 052007
Beacom J. F., 2010, Ann. Rev. Nucl. Part. Sci., 60, 439
Beacom J. F., Vagins M. R., 2004, Phys. Rev. Lett., 93, 171101
Beacom J. F. et al., 2017, Chin. Phys. C, 41, 023002
Bethe H. A., Wilson J. R., 1985, ApJ, 295, 14
Bethe H. A., Brown G. E., Applegate J., Lattimer J. M., 1979a, Nucl. Phys. A, 324, 487
Bisnovatyi-Kogan G. S., Seidov Z. F., 1984, Ann. New York Acad. Sci., 422, 319
Biteau J., Williams D. A., 2015, ApJ, 812, 60
Branch D., Wheeler J. C., 2017, Supernova Explosions. Springer, Berlin, Germany
Burrows A., Vartanyan D., 2021, Nature, 589, 29
Byrne R. A., Fraser M., 2022, MNRAS, 514, 1188
Calzetti D., 2013, Star Formation Rate Indicators. Cambridge University Press, Cambridge, England, p. 419
Cappellari M. et al., 2012, Nature, 484, 485
Cappellaro E. et al., 2015, A&A, 584, A62
Cardelli J. A., Clayton G. C., Mathis J. S., 1989, ApJ, 345, 245
Chabrier G., 2003, PASP, 115, 763
Chabrier G., Hennebelle P., Charlot S., 2014, ApJ, 796, 75
Chakraborty S., Hansen R., Izaguirre I., Raffelt G., 2016, Nucl. Phys. B, 908, 366
Chandrasekhar S., 1931, ApJ, 74, 81
Chomiuk L., Povich M. S., 2011, AJ, 142, 197
Chruślińska M., Jeřábková T., Nelemans G., Yan Z., 2020, A&A, 636, A10
Colgate S. A., White R. H., 1966, ApJ, 143, 626
Couch S. M., 2017, Phil. Trans. R. Soc. A, 375, 20160271
Creque-Sarbinowski C., Hyde J., Kamionkowski M., 2021, Phys. Rev. D, 103, 023527
Dahlen T., Strolger L.-G., Riess A. G., Mattila S., Kankare E., Mobasher B., 2012, ApJ, 757, 70
Das A., Sen M., 2021, Phys. Rev. D, 104, 075029
Davies B., Beasor E. R., 2020, MNRAS, 496, L142
de Gouvêa A., Martinez-Soler I., Perez-Gonzalez Y. F., Sen M., 2020, Phys. Rev. D, 102 , 123012
de Gouvêa A., Martinez-Soler I., Perez-Gonzalez Y. F., Sen M., 2022, preprint (arXiv e-print)
Driver S. P. et al., 2011, MNRAS, 413, 971
Driver S. P. et al., 2018, MNRAS, 475, 2891
Duan H., Fuller G. M., Qian Y.-Z., 2010, Ann. Rev. Nucl. Part. Sci., 60, 569
El Hedri S., Ashida Y., Giampaolo A., 2021, in Kappes A., Keilhauer B., eds, 37th International Cosmic Ray Conference. Diffuse Supernova Neutrino Background Search at Super-Kamiokande, Proceedings of Science, Berlin, Germany, p. 1139
Ertl T., Janka H.-T., Woosley S. E., Sukhbold T., Ugliano M., 2016, ApJ, 818, 124
Fardal M. A., Katz N., Weinberg D. H., Davé R., 2007, MNRAS, 379, 985
Farzan Y., Palomares-Ruiz S., 2014, J. Cosmol. Astropart. Phys., 2014, 014
Ferré-Mateu A., Vazdekis A., de la Rosa I. G., 2013, MNRAS, 431, 440
Ferreras I., Barbera F. L., Rosa I. G. D. L., Vazdekis A., Carvalho R. R. D., Falcón-Barroso J., Ricciardelli E., 2012, MNRAS, 429, L15
Fioc M., Rocca-Volmerange B., 2019, A&A, 623, A143
Fishbach M., Holz D. E., Farr W. M., 2018, ApJ, 863, L41
Fogli G. L., Lisi E., Mirizzi A., Montanino D., 2004, Phys. Rev. D, 70, 013001
Fontanot F., De Lucia G., Hirschmann M., Bruzual G., Charlot S., Zibetti S., 2017, MNRAS, 464, 3812
Fontanot F., Lucia G. D., Xie L., Hirschmann M., Bruzual G., Charlot S., 2018, MNRAS, 475, 2467
Freese K., Rindler-Daller T., Spolyar D., Valluri M., 2016, Rep. Prog. Phys., 79 , 66902
Fuller G. M., 1982, ApJ, 252, 741
Garching Core-Collapse Supernova Archive, 2022
Geha M., 2013, A Non-Universal Initial Mass Function in the Ultra-Faint Galaxy Coma Berenices, HST Proposal ID 13449. Cycle 21
Gerke J. R., Kochanek C. S., Stanek K. Z., 2015, MNRAS, 450, 3289
Goldberg H., Perez G., Sarcevic I., 2006, J. High Energy Phys., 2006, 023
Gruppioni C. et al., 2013, MNRAS, 432, 23
Gunawardhana M. L. P. et al., 2011, MNRAS, 415, 1647
Harayama Y., Eisenhauer F., Martins F., 2008, ApJ, 675, 1319
Heger A., Fryer C. L., Woosley S. E., Langer N., Hartmann D. H., 2003, ApJ, 591, 288
Hopkins A. M., 2018, Publ. Astron. Soc. Aust., 35 , e039
Hopkins A. M., Beacom J. F., 2006, ApJ, 651, 142
Horiuchi S., Beacom J. F., Dwek E., 2009, Phys. Rev. D, 79, 083013
Horiuchi S., Beacom J. F., Kochanek C. S., Prieto J. L., Stanek K. Z., Thompson T. A., 2011, ApJ, 738, 154
Horiuchi S., Beacom J. F., Bothwell M. S., Thompson T. A., 2013, ApJ, 769, 113
Horiuchi S., Nakamura K., Takiwaki T., Kotake K., Tanaka M., 2014, MNRAS, 445, L99
Horiuchi S., Sumiyoshi K., Nakamura K., Fischer T., Summa A., Takiwaki T., Janka H.-T., Kotake K., 2018, MNRAS, 475, 1363
Horiuchi S., Kinugawa T., Takiwaki T., Takahashi K., Kotake K., 2021, Phys. Rev. D, 103, 043003
Ivezić Ž. et al., 2019, ApJ, 873, 111
Janka H.-T., 2017, Neutrino-Driven Explosions. Springer International Publishing, Cham, p. 1095
Jeong Y. S., Palomares-Ruiz S., Reno M. H., Sarcevic I., 2018, J. Cosmol. Astropart. Phys., 06, 019
Jeřábková T., Hasani Zonoozi A., Kroupa P., Beccari G., Yan Z., Vazdekis A., Zhang Z.-Y., 2018, A&A, 620, A39
Keehn J. G., Lunardini C., 2012, Phys. Rev. D, 85, 043011
Keil M. T., 2003, preprint (arXiv:astro-ph/0308228)
Keil M. T., Raffelt G. G., Janka H.-T., 2003, ApJ, 590, 971
Kennedy G. M., Wyatt M. C., Kalas P., Duchene G., Sibthorpe B., Lestrade J.-F., Matthews B. C., Greaves J., 2013, MNRAS, 438, L96
Kennicutt Robert C. J., 1998, ARA&A, 36, 189
Kennicutt R. C., Evans N. J., 2012, ARA&A, 50, 531
Kobayashi C., 2010, in Debattista V. P., Popescu C. C., eds, AIP Conf. Ser. Vol. 1240, Hunting for the Dark: the Hidden Side of Galaxy Formation. Am. Inst. Phys., New York, p. 123
Kochanek C. S., Beacom J. F., Kistler M. D., Prieto J. L., Stanek K. Z., Thompson T. A., Yüksel H., 2008, ApJ, 684, 1336
Koekemoer A. M. et al., 2019, BAAS, 51, 550
Krauss L. M., Glashow S. L., Schramm D. N., 1984, Nature, 310, 191
Kresse D., Ertl T., Janka H.-T., 2021, ApJ, 909, 169
Kroupa P., 2001, MNRAS, 322, 231
Kroupa P., Weidner C., 2003, ApJ, 598, 1076
Larson R. B., 1998, MNRAS, 301, 569
Lattimer J. M., Swesty F. D., 1991, Nucl. Phys. A, 535, 331
Laureijs R. et al., 2011, Euclid Definition Study Report, preprint (arXiv:1110.3193)
La Barbera F. et al., 2019, MNRAS, 489, 4090
Leitherer C. et al., 1999, ApJS, 123, 3
Li A., Draine B. T., 2001, ApJ, 554, 778
Libanov A., Sharofeev A., 2022, preprint (arXiv e-print)
Lien A., Fields B. D., Beacom J. F., 2010, Phys. Rev., D81, 083001
Li Y.-F., Vagins M., Wurm M., 2022, Universe, 8, 181
Lunardini C., 2009, Phys. Rev. Lett., 102, 231101
Lunardini C., 2016, Astropart. Phys., 79, 49
Lunardini C., Tamborra I., 2012, J. Cosmol. Astropart. Phys., 2012, 012
Madau P., Dickinson M., 2014, ARA&A, 52, 415
Magnelli B. et al., 2013, A&A, 553, A132
Magnelli B., Elbaz D., Chary R. R., Dickinson M., Le Borgne D., Frayer D. T., Willmer C. N. A., 2011, A&A, 528, A35
Malek M. et al., 2003, Phys. Rev. Lett., 90 , 61101
Maoz D., Mannucci F., Nelemans G., 2014, ARA&A, 52, 107

Mathews G. J., Hidaka J., Kajino T., Suzuki J., 2014, ApJ, 790, 115
Mattila S. et al., 2012, ApJ, 756, 111
Mazzali P. A., Ropke F. K., Benetti S., Hillebrandt W., 2007, Science, 315, 825
Mirizzi A., Tamborra I., Janka H.-T., Saviano N., Scholberg K., Bollig R., Hudepohl L., Chakraborty S., 2016, Riv. Nuovo Cim., 39, 1
MØller K., Suliga A. M., Tamborra I., Denton P. B., 2018, J. Cosmol. Astropart. Phys., 2018, 066
Nakazato K., 2013, Phys. Rev. D, 88, 083012
Nakazato K., Mochida E., Niino Y., Suzuki H., 2015, ApJ, 804, 75
Neustadt J. M. M., Kochanek C. S., Stanek K. Z., Basinger C., Jayasinghe T., Garling C. T., Adams S. M., Gerke J., 2021, MNRAS, 508, 516
Offner S. S. R., Clark P. C., Hennebelle P., Bastian N., Bate M. R., Hopkins P. F., Moreaux E., Whitworth A. P., 2014, Protostars and Planets VI, University of Arizona Press, Tucson, Arizona
Padoan P., Nordlund A., Jones B. J. T., 1997, MNRAS, 288, 145
Perrett K. et al., 2012, AJ, 144, 59
Petrushevska T. et al., 2016, A&A, 594, A54
Priya A., Lunardini C., 2017, J. Cosmol. Astropart. Phys., 2017, 031
Razzaque S., Dermer C. D., Finke J. D., 2009, ApJ, 697, 483
Regős E., Vinkó J., 2019, ApJ, 874, 158
Rose B. M. et al., 2021, A Reference Survey for Supernova Cosmology with the Nancy Grace Roman Space Telescope, Cornell, Ithaca, NY
Salpeter E. E., 1955, ApJ, 121, 161
Sawatzki J., Wurm M., Kresse D., 2021, Phys. Rev. D, 103, 023021
Sharda P., Krumholz M. R., 2021, MNRAS, 509, 1959
Singh R., Rentala V., 2021, J. Cosmol. Astropart. Phys., 2021, 019
Smith N., 2014, ARA&A, 52, 487
Strolger L.-G. et al., 2015, ApJ, 813, 93
Strolger L.-G., Rodney S. A., Pacifici C., Narayan G., Graur O., 2020, ApJ, 890, 140
Sukhbold T., Ertl T., Woosley S. E., Brown J. M., Janka H.-T., 2016, ApJ, 821, 38
Suliga A. M., Beacom J. F., Tamborra I., 2022, Phys. Rev. D, 105, 043008
Tabrizi Z., Horiuchi S., 2021, J. Cosmol. Astropart. Phys., 2021, 011
Tamborra I., Shalgar S., 2021, Ann. Rev. Nucl. Part. Sci., 71, 165
Tamborra I., Muller B., Hudepohl L., Janka H.-T., Raffelt G., 2012, Phys. Rev. D, 86, 125031
Turatto M., 2003, Lecture Notes in Physics. Vol. 598, Springer Berlin Heidelberg, Germany, p. 21
van Dokkum P. G., Conroy C., 2010, Nature, 468, 940
van Son L. A. C. et al., 2022, ApJ, 931, 17
Vitale S., Farr W. M., Ng K. K. Y., Rodriguez C. L., 2019, ApJ, 886, L1
Weingartner J. C., Draine B. T., 2001, ApJ, 548, 296
Wilkins S. M., Trentham N., Hopkins A. M., 2008a, MNRAS, 385, 687
Wilkins S. M., Hopkins A. M., Trentham N., Tojeiro R., 2008b, MNRAS, 391, 363
Wilkins S. M., Lovell C. C., Stanway E. R., 2019, MNRAS, 490, 5359
Wilson J. R., Mayle R., Woosley S. E., Weaver T., 1986, Ann. New York Acad. Sci., 470, 267
Zhang H. et al., 2015, Astropart. Phys., 60, 41
Zubko V., Dwek E., Arendt R. G., 2004, ApJS, 152, 211

APPENDIX A: SUPERNOVA NEUTRINO SPECTRA

In order to estimate the DSNB flux, we model the CCSN population by relying on the outputs of one-dimensional, hydrodynamic supernova simulations with Boltzmann neutrino transport from the Garching group (Garching Core-Collapse Supernova Archive 2022). Following Møller et al. (2018), three reference CCSN models are used to account for the variations in neutrino emission depending on the mass and fate of the progenitor star. For CCSNe leading to the formation of a neutron star as the compact object remnant, we use models with initial masses of 9.6 and 27 $M_\odot$, whereas for stellar collapses leading to the formation of black holes, we use the 40 $M_\odot$ 'low' mass accretion rate model (Mirizzi et al. 2016). In all three models, the nuclear equation of state is assumed to be that of Lattimer and Swesty, with a nuclear incompressibility modulus $K =$ 220 MeV (LS220 EoS; Lattimer & Swesty 1991).

The related neutrino energy distributions are well described by a pinched Fermi–Dirac distribution (Keil 2003; Keil, Raffelt & Janka 2003; Tamborra et al. 2012):

$$\left(\frac{\mathrm{d}n}{\mathrm{d}E}\right)_{\bar{\nu}_e} = E_\nu^{\mathrm{tot}} \frac{(1+a)^{1+a}}{\Gamma(1+a)} \frac{E^a}{\langle E_\nu\rangle^{2+a}} e^{\left[-(1+a)\frac{E}{\langle E_\nu\rangle}\right]}. \tag{A1}$$

Here, the parameters E_ν^{tot}, a, and $\langle E_\nu\rangle$ represent the total energy emitted in (anti-electron) neutrinos; a parameter that describes the spectral shape, related to the pinching parameter; and the average energy of the emitted neutrinos, respectively.

While the mean energy, luminosity (energy emitted per time), and pinching parameter are time-dependent quantities, we are interested in the time-integrated neutrino energy distributions. Therefore, we report the time-integrated characteristic quantities in Table A1 for all three models adopted to model the DSNB and show these energy spectra in Fig. A1. Note that these simulations do not include the effects of neutrino flavor mixing, which we do not take into account throughout this work.

Table A1. Best-fitting parameters for the pinched Fermi–Dirac distribution used to describe the numerically generated time-integrated neutrino spectra.

	E_ν^{tot} [MeV]	a	$\langle E_\nu\rangle$ [MeV]
Neutron star (10 $M_\odot$)	1.890×10^{58}	2.355	12.620
Neutron star (27 $M_\odot$)	3.435×10^{58}	2.307	13.856
Black hole (40 $M_\odot$)	4.426×10^{58}	2.083	17.943

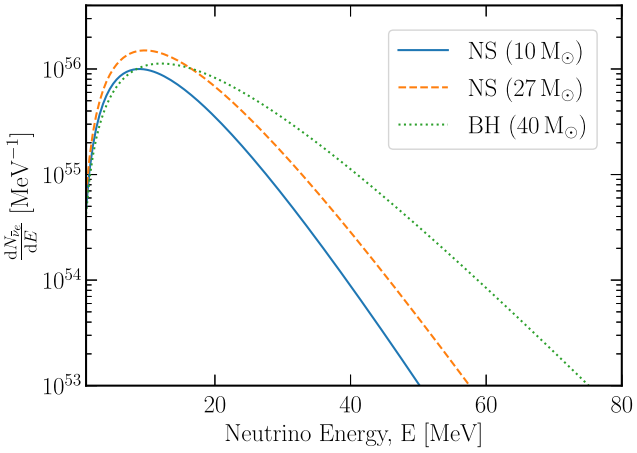

Figure A1. Electron antineutrino energy spectra at the source: Here, we show the time-integrated anti-electron neutrino emission spectra of the three reference CCSN models that we use in this work. The blue solid and orange dashed curves correspond to supernovae that result in neutron stars, whose stellar progenitors have 9.7 and 27 $M_\odot$ masses, respectively. The green dotted curve represents a supernova that results in the formation of a black hole and whose stellar progenitor has a mass of 40 $M_\odot$. Note that these are the spectra at the source; when observed, these spectra will be redshifted by a factor $1 + z$, so that supernovae at high redshift only have non-negligible contributions to the observed spectra at low energies.

This paper has been typeset from a TEX/LATEX file prepared by the author.